Indian Journal of Engineering & Materials Sciences
Vol. 29, August 2022, pp. 437-444
DOI: 10.56042/ijems.v29i4.48695

Synthesis of diamagnetic ZnO nano-crystallites via sol-gel method and their photocatalytic activity

Deepak Kumar, & Mohan Singh Mehata*

Laser-Spectroscopy Laboratory, Department of Applied Physics, Delhi Technological University, Bawana Road, Delhi 110 042, India

Received: 9 April, 2021; Accepted: 30 July 2021

The diamagnetic zinc oxide (ZnO) nano-crystallites were synthesized via the sol-gel method. The X-ray diffraction (XRD) and field emission scanning electron microscope (FESEM) were used for structural characterization. The XRD pattern demonstrates that the ZnO nanoparticles (NPs) have a wurtzite structure with an average crystallite size of ~20 nm. TheFESEM and EDAX (energy- dispersive x-ray analysis) confirm the particles are in granular, spherical, and rod-like mixed-phase. The absorption spectra show a red shift and observed bandgap energy of about 3.17 eV, which might attribute because of the oxygen vacancies. Further, photoluminescence (PL) exhibits dual peaks at wavelengths 430 and 550 nm, which maybe due to defects induced at the surface of the NPs. The vibrating sample magnetometer (VSM) study demonstrates the diamagnetic behavior of zinc oxide nanoparticles at 300 K. The photocatalytic effectiveness of the ZnO NPs was examined by decomposing a congo red (CR) dye as an organic water pollutant under UV irradiation. The leading absorption peak of CR dye decreases with the UV irradiation time. The complete decolorization of the CR dye was observed after 150 min with the reaction rate constant of 0.018 min^{-1}.

Keywords: Zinc oxide, Photoluminescence, Synthesis, Photocatalytic activity, Diamagnetic behavior, Scavenged

1 Introduction

The material zinc oxide (ZnO) has played a vital role in various sectors of the ever-growing research field. The ZnO is an (II-IV) semiconductor material, possessing wide bandgap energy of 3.3 eV at ambient temperature and pressure with large excitons (60 meV)[1]. It is found in two common polytypes, i.e., cubic zinc and blende hexagonal Wurtzite. The Wurtzite phase having tetrahedral coordination, which exhibits sp^3 covalent bonding, is the most stable phase underfavorable conditions. It has outstanding multifunctional material properties, such as high chemical and photostability, a wide range of radiation absorption, wide bandgap, and cheap and non-toxic. In past decades, researchers paid serious attention to the ZnO for its magnificent properties, which could be employed in various applications like in spintronic, optoelectronic, piezoelectric, and photochemical materials[2], superconductors[3], photocatalyst[4], magnetic[5], light-emitting diodes[6] and biological applications[7].

Various techniques were used to process different types of ZnO nanostructures, including sol-gel technique, co-precipitation, chemical vapour deposition, hydrothermal method, *etc.*[8-9] and solved the purposes. The sol-gel approach proved the most favorable because it is very pocket-friendly, facile, and produces a scalable amount of nanoparticles. The properties and the application of ZnO depend primarily on its shape, size, and structure. The spherical nanostructures of ZnO are mainly exploited for their photocatalytic activities[10].

In this era of industrialization, the increasing demand for products like textiles, toiletries, healthcare, food, beverages, and other industries has led to the release of highly toxic organic compounds like dyes untreated into the water bodies. This causes the destruction of natural reserves of water (rivers, lakes, etc.), which has a long-lasting adverse effect on humanity and the aquatic ecosystem. One such commonly used synthetic dye is the CR dye, an anionic azo and water-soluble red dye used in textile and leather industries. The presence of a meager amount of the compound could lead to chronic carcinogenic diseases in human beings. This industrial pollutant can cause severe environmental effluences such as water pollution, destruction of water plants, and extinction of aquatic life because of the colorization of the water bodies by the dye extracts discarded directly to rivers through sewage.

Over the past few decades, a tremendous increase in the efforts has been employed for eco-friendly

* Corresponding author (E-mail: msmehata@gmail.com)

ways to remove the dye's waste from the water through photocatalytic activity[11]. Many different photocatalytic materials have been developed and used to eliminate CR from sewage waste. The photocatalytic activities of Metal Oxide Semiconductors (MOSs) are preferred because of their efficient adsorption and photocatalytic properties[12]. When the MOSs is transformed into nanoparticles, they exhibit unique physicochemical and biological properties because of the enhancement in surface area to volume ratio.

The ZnO had always been the first choice for photocatalytic decomposition of organic contaminants[13]. The pristine ZnO nanomaterials have been produced via the sol-gel method and employed directly to decompose the congo red dye in the current work. The elaborated structural, morphology and optical study have been investigated for the ZnO-based photocatalytic activity.

2 Materials and Methods

All the high purity chemicals were of analytical grades, such as zinc acetate dihydrate ($(CH_3COO)_2Zn).2H_2O$) bought from Sigma-Aldrich with a purity of 99.99%. Sodium hydroxide (NaOH) has been purchased from the CDH and used without further purification. The de-ionized (DI) water (specific resistivity: 18.2 MΩ·cm) was used as the medium.

4.24 gm of zinc acetate dihydrate powders were dispersed in 100 ml DI and then kept on the magnetic stirrer (900 rpm) for 30 minutes. Simultaneously, 4.0 gm of NaOH was mixed with 50 ml of DI and kept on the magnetic stirrer (800 rpm) for 15 min. We obtained the two clear solutions from the above procedure then the NaOH solution was mixed drop wise in the zinc acetate solution under vigorous stirring for 1 h. The precipitate (white color gel) was formed and left to settle. The residue was washed and filtered four times with DI and ethanol (1:1). It was heated in an oven at 60 °C for 120 min to remove wetness from the precipitate. The dried NPs were calcined at 300 °C for 180 min to get the desire ZnO NPs.

X-ray diffraction (XRD) analysis by Bruker 8D Advance having Cu Kα (1.54 Å) source radiation with an accelerating voltage of 0.04 MV and current of 0.02 Amp. The absorption and reflectance spectra were analyzed with a spectrometer (Perkin Elmer, dual-beam Lambda-750, UV/VIS/NIR). The Photoluminescence (PL) spectra analysis with the Spectrofluorometer Horiba USA (Fluorolog-3), equipped with a double grating at emission and excitation monochromators[14]. The structural morphology and elemental compositions of the samples were obtained using the field emission scanning electron microscope (FESEM, ZEISS Microscope MA15/18) images and energy-dispersive X-ray spectrum analysis (Model EDS 51N1000). VSM (Vibrating Sample Magnetometer) was used to examine the magnetic nature of the produced ZnO NPs.

3 Results and Discussion

The X-ray diffraction patterns depict the structural information about the ZnO, which attributes to the diffraction peaks at Bragg angles of (2θ) 31.76°, 34.42°, 36.25°, 47.53°, 56.59°, 62.85°, 66.374°, 67.94°, 69.08°, that correspond to (100), (002), (101), (102), (110), (103), (200), (112), (201) crystal plane, respectively as shown in Fig. 1. The peaks demonstrated ZnO nanoparticle formation with hexagonal Wurtzite crystal structure, following the standard spectrum of JCPDS Card No. 00-036-1451. The diffraction patterns indicate no impurities exist in the standard hexagonal Wurtzite structure[15]. Using Scherrer's formula Eq. (1), the average crystallite size was estimated (~20 nm) the ZnO peaks ((110), (002))[16].

$$D = \frac{0.9\lambda}{\beta \cos\theta} \quad \ldots (1)$$

where, λ is the X-ray source wavelength (CuKα having λ = 0.154 nm) and 'β' is the full width of the angular peak at the half maximum (Radian), θ is the Bragg's diffraction angle. Using Eq. (2), the lattice parameters, a=b and c, of ZnO nanoparticles were calculated to be 3.245 and 5.196 Å[17].

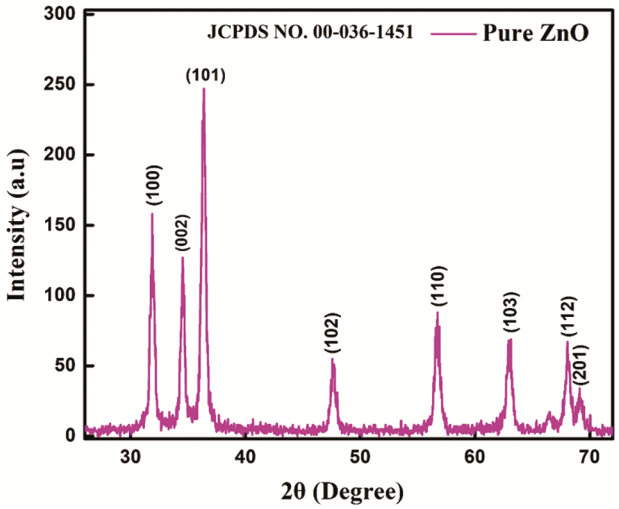

Fig. 1 — X-ray diffraction pattern of ZnO NPs.

$$\frac{1}{d_{hkl}^2} = \frac{4}{3}\left(\frac{h^2+hk+k^2}{a^2}\right) + \frac{l^2}{c^2} \quad \ldots (2)$$

where, the miller indices (h,k,l), inter-planar spacing 'd'. The values of 'a' and 'c' were calculated by (110) and (002) crystal planes corresponding to the peak position of 56.59° and 34.42°. The atomic packing factor (APF) ratio (c/a) and the cell volume of the lattice of the ZnO in the tetrahedral coordination were calculated to be 1.60 and 47.38 (Å)^{3,} respectively[18]. The bond length of all the samples was estimated using Eqs. (3) and (4) came out to be 1.97Å[19].

$$u = \left(\frac{a^2}{3c^2} + 0.25\right) \quad \ldots (3)$$

$$L = \sqrt{\frac{a^2}{3} + \left(\frac{1}{2} - u^2\right)^2 c^2} \quad \ldots (4)$$

The positional parameter 'u' (~0.38) is calculated from Eq. (3). The ionic characteristics and distortion of all the NPs were identified by positional parameters[20]. The crystallite size is inversely proportional to the dislocation density (δ) and how much defect exists in the NPs. The dislocation density (2.5×10^{-3} nm^{-2}) was determined by using Eq. (5)[21],

$$\delta = \frac{1}{D^2} \quad \ldots (5)$$

where, 'D' is the crystallite size obtained from the XRD results. Variation of crystallite size depends on $1/Cos\theta$, while strain with tanθ, and both, in turn, depend on diffraction angle θ. The crystal imperfection and distortion in powder cause strain-induced broadening calculated using Williamson-Hall (W-H) method Eq. (6)[22],

$$\varepsilon = \frac{\beta Cos\,\theta}{4\,Sin\theta} \quad \ldots (6)$$

The microstrain (ε), and dislocation density (δ) of the nanoparticles are more prominent as compared to the crystallite size (D). It may be because of the lattice contractions[23]. The W-H plot of synthesized NPs $\beta cos\,\theta$ (y- axis) vs. $4\,sin\theta$ (x- axis) are presented in the Fig. 2. The degree of distortion 'R' was evaluated by Eq. (7), where a, c are lattice constants.

$$R = \frac{2a(2\div3)^{1/2}}{c} \quad \ldots (7)$$

To verify all the sample's structure is an ideal Wurtzite structure, the degree of distortion value should be unity[24]. The calculated R-values were approximately found to be 1.02

The FESEM images of the nanoparticles are shown in Fig. 3(a) and display the particles are in granular

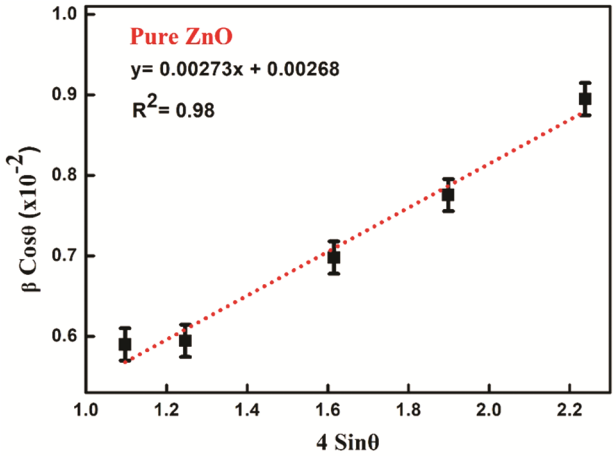

Fig. 2 — The W-H plot between βcosθ *vs.* 4sinθ of synthesized ZnO NPs.

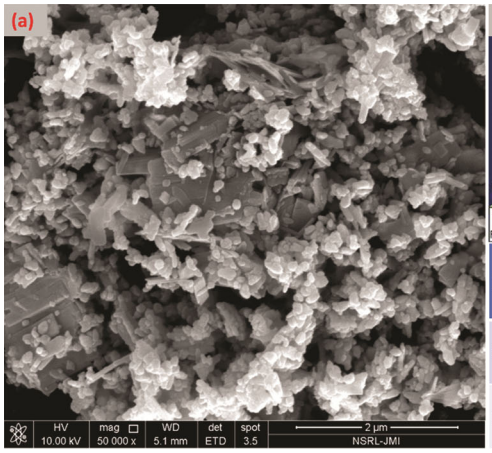

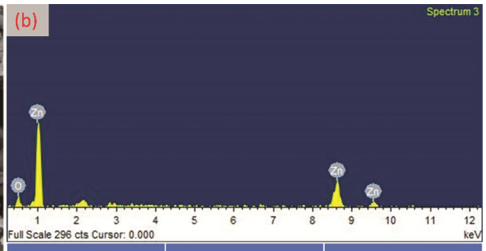

Element	Weight%	Atomic%
O	14.11	40.16
Zn	85.89	59.84

Fig. 3 — ZnO NPs (a) FESEM image, and (b) EDAX spectrum.

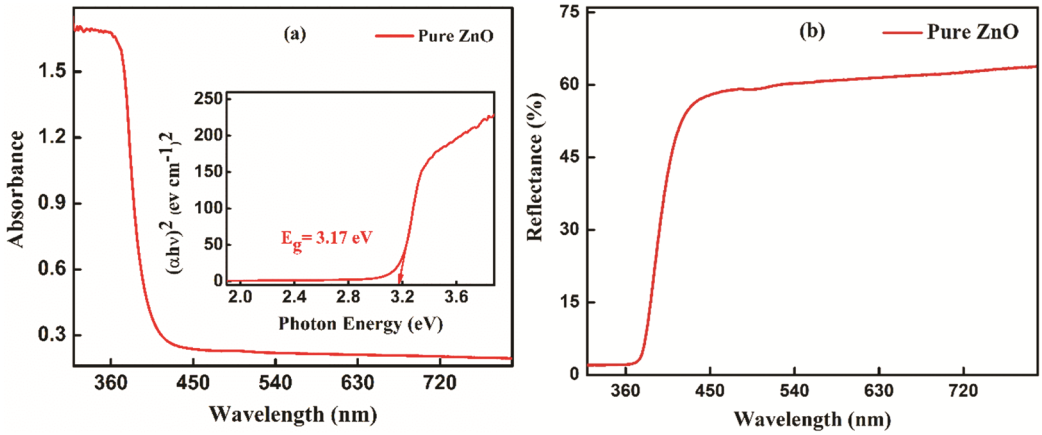

Fig. 4 — (a) The absorption spectrum along with the Tauc plot (inset) corresponds to the direct bandgap, and (b) diffuse reflectance spectrum of the ZnO NPs.

nature, spherical and rod-like mixed-phase (hexagonal and spherical)[25]. The particle size of the ZnO was measured and found to be 54 nm. The elemental compositional analysis was confirmed by the EDAX spectroscopy of the NPs, as shown in Fig. 3(b), which depicts that the Zn and O elements are the leading entities in the sample of ZnO NPs and there were no other fundamental peaks observed in the EDAX spectra.

The absorption and reflectance spectra of ZnO NPs were explored in the wavelength range of 200 to 800 nm at ambient temperature and pressure, as presented in Fig. 4 (a and b). Using the well-known Tauc plot relation Eq. (8), the calculated optical bandgap energy is 3.13 eV[26]. The plot of '$(\alpha hv)^2$ and vs. hv for pure ZnO NPs is shown in Fig. 4 (a).

$$\alpha hv = A\left(hv - E_g\right)^n \quad \ldots (8)$$

E_g represents the bandgap energy of the specimen, α is the absorption coefficient, A is the constant, hv is the incident photon energy, n is the transition coefficient and the value of n depends on the inherent characteristics of semiconductor materials[27]. The values of n = 1/2, 3/2, 2 and 3 represent the direct bandgap, forbidden direct bandgap, indirect bandgap, and forbidden indirect transition gap, respectively.

Nowadays, modern technology is moving towards the design and fabrication section, fabrication of the optoelectronic and integrated circuit (IC) components on the scale of 7, 5, 3 nm and smaller as possible are required. Therefore, it is essential to calculate and compare the bandgap and Refractive Index (RI) of the materials to design and fabricate such sections. Electronic, optical, and optoelectronic applications of semiconductor materials usually depend on their refractive index and bandgap energy. The energy gap measures the photon absorption threshold, whereas the refractive index measures transparency to the incident photons[28]. To determine the refractive index, many empirical relations were proposed[29]. Moss[29] proposed the first relation in 1950 with the known energy gap of semiconductor materials. Five empirical relationships were used to evaluate the refractive index Eq. (9) with the known bandgap (3.17 eV). Suppose the bandgap value of the materials is very small or large. In that case, the relation[29] is not well suited for the calculation of the RI and fits for the range of the energy gap 0.5 eV <Eg< 3.68 eV of the materials[29].

$$n = \left(\frac{95}{\mathrm{Eg}}\right)^{\frac{1}{4}} \quad \ldots (9)$$

Eq. (10)[30-31] validates if the value of energy gap falls in between the range 1.5eV <Eg< 3.50 eV and the theory failed for the values in the region other than this, i.e., if Eg> 6.587 eV and gives negative value[28-30-31].

$$n = 4.084 - 0.63\mathrm{Eg} \quad \ldots (10)$$

The relation Eq. (11) at low and high values of the energy gap[32] provided nearly the same value as obtained from the Moss relation. The expression failed when the energy gap is Eg< 1.4 eV; however, Eq. (10) is reliable in the range of 2.0 eV <Eg< 4.0 eV.

$$n = \sqrt{1 + \left(\frac{13.6}{\mathrm{Eg}+3.47}\right)^2} \quad \ldots (11)$$

The modified Moss relation Eq. (12), in which the constant value of 0.365 was subtracted from the energy gap, yielded a better result than Eq. (9)[33-34]. This relation not valid when bandgap is about 0.365 eV but valid for the range of 1.10 eV <Eg< 6.20 eV.

$$n = \left(\frac{154}{\mathrm{Eg}-0.365}\right)^{\frac{1}{4}} \quad \ldots (12)$$

Kumar and Singh[35] reported in Eq. (13) that when the energy gap is at a lower value, its refractive index lies between the Moss and Reddy relation. While at a higher value of Eg, it lies below the Reddy relation and higher in the Moss relation. The typical reliable rage is 2.00 eV <Eg< 4.00 eV[36-37].

$$n = 3.3668(\mathrm{Eg})^{-0.3228} \quad \ldots (13)$$

Above all, the relation gives a better result when the energy gap lies between the ranges of 2.0 eV to 4.0 eV. Thus, the refractive index values of the ZnO NPs were calculated from the given above five relations Eqs (9 - 13). The refractive index estimated from Moss relation is (2.33) whereas from Kumar & Singh[35] to be (2.32), nearly the same. The highest refractive index of NPs is 2.72 was calculated through the Reddy and Anjayenulu[23] relations, while the lowest refractive index (2.08) of NPs by Ravindra *et al*[31]. The moderate RI was calculated by Harve *et al*[32]. is (2.27).

PL spectra provide information about excited states and their energy and the presence of defects and trap states. The spectral intensity is associated directly with the defect density or structural defects in the semiconductors[38]. The PL spectrum of ZnO NPs has been measured in the wavelength range of 200 to 800 nm at the excitation wavelength of 320 nm at ambient conditions and illustrated in Fig. 5. A broad PL spectrum is observed with a band maximum at 540 nm. The Gaussian bands (G1 and G2) well reproduce the PL spectrum. G1 appeared at 434 nm and G2 at 540 nm. These bands are well-matched with the reported values[39-40]. The G1 band, which is located at around 434 nm, originated from the direct bandgap energy, i.e., the recombination of electrons (e^-) from the conduction band (CB) to the zinc vacancies (V_{zn})

Whereas the relative stronger band observed at 540 nm related to the oxygen vacancies (V_O) and zinc interstitials (Zn_i), or transition from the valence band to the oxygen vacancies (V_O) and zinc interstitials (Zn_i).

The magnetic characteristics of the synthesized ZnO NPs were measured at 300 K via a vibrating sample magnetometer. The M-H curve of the NPs exhibited diamagnetic nature, as shown in Fig. 6. The purely diamagnetic behavior of the ZnO at the low applied magnetic field supports the presence of oxygen vacancies (V_O) and zinc vacancies (V_{zn}), as described by PL spectrum. Besides, the lattice distortion and the size effect can also be responsible for the diamagnetic magnetic behavior of the NPs[41].

The photocatalytic activity (PCA) of ZnO was tested for the photodegradation of an anionic congo red (CR) azo dye under UV irradiation. For the study, the dye concentration was chosen to be 5.0×10^{-5} M. Figure 7 (a) shows the absorption of the CR dye in

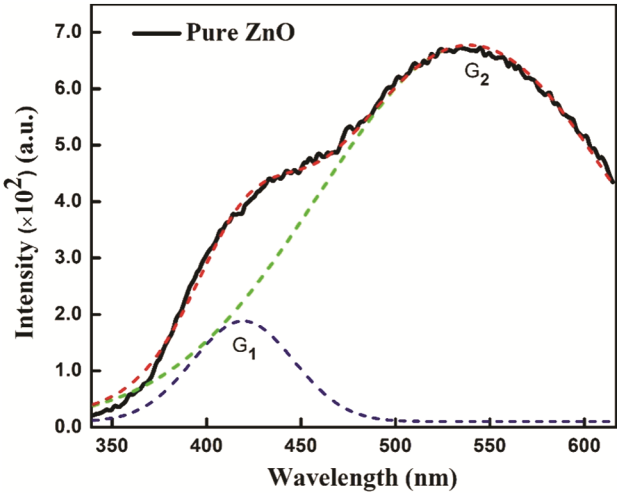

Fig. 5 — The photoluminescence spectrum (solid red line) of ZnO NPs and G_1 and G_2 Gaussian bands (dotted blue and green line) along with the fitted curve (red dotted line). The excitation wavelength (λ_{ex}) was 320 nm.

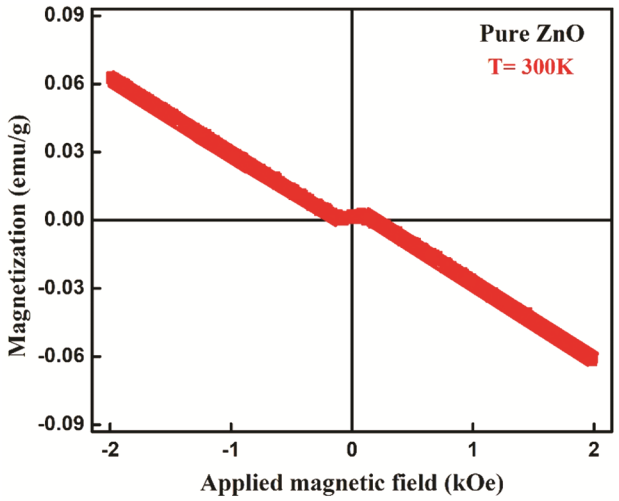

Fig. 6 — M-H curve of ZnO NPs at the 300 K.

water. The maximum absorption corresponding to the lowest energy band is at 498 nm. The blank CR dye solution (without a mixture of ZnO catalyst) was kept under UV irradiation to examine the photolytic reaction. Still, there was no effect, hence no decomposition of dye without catalysts. Then, the typical dye degradation was performed in the presence of ZnO NPs as a catalyst (0.8 gL^{-1}) in an aqueous medium.

In this process, the catalyst (ZnO NPs) was initially added to the dye solution and stirred in the dark for 1 h to reach the adsorption-desorption isotherm. Then 4 ml of the mixed solution was extracted from the sample and centrifuged at 7000 rpm for 2 min. The sample's absorption spectra were recorded before and after the exposure with UV illumination at specific intervals. Before photoirradiation, the CR dye was degraded slowly, and the rate became extremely slow after some intervals, i.e., the change in absorption is nearly minimal (Fig. 7(a)). After that, the specimen was kept under a UV lamp of 8 Watts, λ ~ 254 nm, and 1.2 mW/cm^2. Upon the photoirradiation, the absorption intensity of CR dye decreases; hence the photodegradation of the dye starts. Upon increasing the photoirradiation time, the absorption intensity gradually decreased and became minimal at an irradiation time of 150 min. The reaction rate constant of dye degradation has been calculated using pseudo-first-order kinetic relation $ln\ (A/A_0) = -kt$[42]. Where 'A_0' and 'A' are the dye absorbance at initial and after a specific irradiation time, respectively. The 'k'is the pseudo-first-order rate constant (min^{-1}), and 't' is the photo-irradiation time (min). The reaction rate constant response is 0.018 min^{-1} obtained from the linear fitted curve. The linear fitted curve is plotted between the $ln\ (A/A_0)$ vs. t (irradiation time) as shown in Fig. 7(b). The degradation efficiency (DE) was estimated by using Eq. (14)[43].

$$\text{Degradation efficiency (DE)}\% = \frac{A_0 - A}{A} \times 100 \quad \ldots (14)$$

The photodegradation efficiency of pure ZnO was calculated to be 98 %.

In the process of PCA, the electron-hole pairs are generated by the exposure of adequate UV light energy (hv) on the ZnO nanoparticles. The generated holes and electrons participate in the decomposition of CR dye, as demonstrated in Fig. 8.

$$ZnO + hv(\text{UV irradiation}) \rightarrow ZnO\ (e^- - h^+) \quad \ldots (15)$$

To produce hydroxyl (·OH), the holes (h^+) are formed when the valence band electrons of the catalyst react with electron donors, i.e., H_2O and hydroxyl ions (OH^-)[44]. In the conduction band, the electrons react with the O_2 (oxygen molecule) on the ZnO surface to produce reactive super radical anions ($\cdot O_2^-$)[45]. In the formation of hydroperoxyl radical ($HO_2\cdot$) and hydrogen peroxide (H_2O_2), the reaction will continue, and finally, the hydroxyl radicals are formed. Thus, the hole (h^+) and hydroperoxyl radicals are highly reactive intermediates attacking dye repeatedly and eventually decomposing the dye or organic pollutants[46-47].

$$\text{Dye} + (HO_2\cdot), (\cdot O_2^-), (OH^\cdot) \rightarrow \text{intermediates} \rightarrow \text{final products} \quad \ldots (16)$$

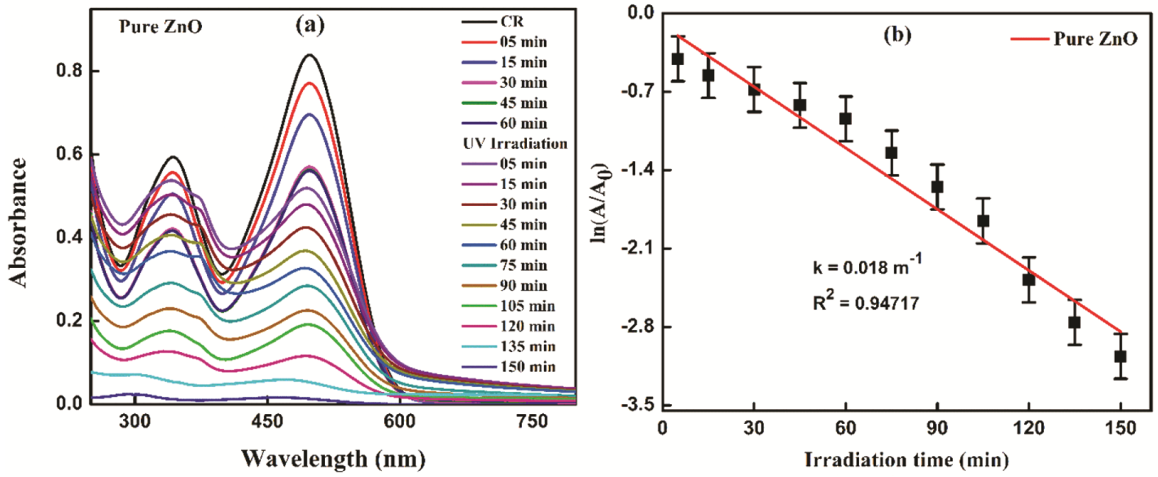

Fig. 7 — (a) The absorption spectra of CR dye in water in the presence of pure ZnO under UV irradiation at different time intervals , and (b) plot of $\ln(A/A_0)$ vs. t (irradiation time).

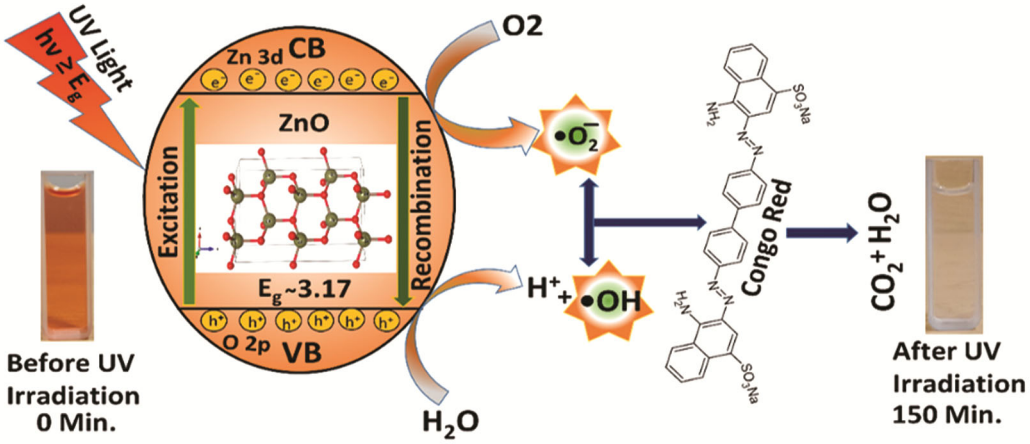

Fig. 8 — Schematic representation of the photocatalytic process and dye degradation in the presence of ZnO nanoparticles.

Nevertheless, trapping e^- in the CB to be scavenged through the e^- acceptors suppresses its recombination with the trapped hole.

4 Conclusion

The pure ZnO NPs were produced via the facile sol-gel method. The structural and elemental investigations of the NPs were carried out with XRD, FESEM with EDAX, UV-vis, PL and VSM. The observed crystallite size of the synthesized NP was ~20 nm. FESEM and EDAX images depict the particles in granular, spherical, and rod-like mixed-phase, and Zn and O elements exist in the ZnO NPs. The bandgap of NPs is ~3.17 eV obtained from the absorption spectrum. The PL spectrum demonstrates that the defects are present in the ZnO, which may be oxygen or zinc vacancy due to which diamagnetic behavior appears in the ZnO NPs. The CR dye degraded under UV irradiation. Within 150 min, the specific amount of the dye degraded entirely with 98% efficiency.

Acknowledgment

DK is thankful to all the lab members for their help, especially Dr. Prateek Sharma.

References

1 Kumar Y, Sahai A, Olive-Méndez S F, Goswami N, & Agarwal V, *Ceram Int,* 42 (2016) 5184.
2 Kariper I A, *Opt Mater,* 44 (2015) 78.
3 Li Y J, Wang C Y, Lu MY, Li K M, & Chen L J, *Cryst Growth Des,* 8 (2008) 2598.
4 Ghosh S S, Choubey C, & Sil A, *Superlattices Microstruct,* 125 (2019) 271.
5 Mesaros A, Ghitulica C D, Popa M, Mereu R, Popa A, Petrisor T, Gabor M, Cadis A I, & Vasile B S, *Ceram Int,* 40 (2014) 2835.
6 Alsharafi R, Zhu Y, Li F, Xu Z, Hu H, & Guo T, *Org Electron,* 75 (2019) 105411.
7 Lima M K, Fernandes D M, Silva M F, Baesso M L, Neto A M, de Morais G R, Nakamura C V, de Oliveira Caleare A, Hechenleitner A A W, & Pineda E A G, *J Sol-Gel Sci Technol,* 72 (2014) 301.
8 Devi P G, & Velu A S, *J Theor Appl Phys,* 10 (2016) 233.
9 Sutanto H, Wibowo S, Hadiyanto, Arifin M, & Hidayanto E, *Mater Res Express,* 4 (2017) 076409.
10 Güy N, Çakar S, & Özacar M, *J Colloid Interface Sci,* 466 (2016) 128.
11 Kumar D, Singh M K, & Mehata M S, *Mater Res Bull,* 150 (2022) 111795.
12 Jamal N, Radhakrishnan A, Raghavan R, & Bhaskaran B, *Main Gr Met Chem,* 43 (2020) 84.
13 Huang Y T, & Shih M C, *Int J Sci Res Publ,* 6 (2016) 549.
14 Mehata M S, & Ratnesh R K, *Dalt Trans,* 48 (2019) 7619.
15 Ji Huang, Cai C, Zhou S, & Liu W, *J Mater Sci Mater Electron,* 29 (2018) 12917.
16 Singh M K, & Mehata M S, *Optik*, 193 (2019) 163011.
17 Hassan F, Miran M, Simol H, Susan M H, & Mollah M, *Bangladesh J Sci Ind Res,* 50 (2015) 21.
18 Islah-u-din, Salam W T, Gillani S S A, Tahir M B, Ikram M, & Ali S, *Optik,* 203 (2020) 163966.
19 He R, Tang B, Ton-That C, Phillips M, & Tsuzuki T, *J Nanoparticle Res,* 15 (2013) 1.
20 Gupta G, Verma S, Nagarajan R, & Rath S, *Phys B & Condens Matter,* 604 (2021) 412735.
21 Srinivasulu T, Saritha K, & Reddy K T R, *Mod Electron Mater,* 3 (2017) 76.
22 Khorsand Zak A, Majid W H Abd, Abrishami M E, & Yousefi R, *Solid & State Sci,* 13 (2011) 251.
23 Tiwari A, & Sahay P P, *Opt Mater*, 110 (2020) 110395.
24 Ran A K, Kumar Y, Rajput P, Jha S N, Bhattacharyya D, & Shirage P M, A*CS Appl Mater Interfa,* 9 (2017) 7691.
25 Thirupathi C, Nithiyanantham S, Sentilkumar M, Arivudainambi A, Mahalakshmi S, & Natarajan B, *Adv Sci Eng Med,* 12 (2020) 524.
26 Singh M K, & Mehata M S, *Ceram Int,* 47 (2021) 32534.
27 Fang M, Tang C M, & Liu Z W, *J Electron Mater,* 47 (2018) 1390.
28 Tripathy S K, *Opt Mater,* 46 (2015) 240.
29 Moss T S, *Phys Status Solidi,* 131 (1985) 415.

30 Gupta V P, & Ravindra N M, *Phys Status Solidi,* 100 (1980) 715.
31 Ravindra N M, Auluck S, & Srivastava V K, *phys stat sol,* 93 (1979) K155-K160.
32 Hervé P, & Vandamme L K J, *Infrared Phys Technol,* 35 (1994) 609.
33 Reddy R R, & Anjaneyulu S, *Phys Status Solidi,* 174 (1992) K91.
34 Reddy R R, & Ahammed Y N, *Infrared Phys Technol,* 36 (1995) 825.
35 Kumar V, & Singh J K, *Indian J Pure Appl Phys,* 48 (2010) 571.
36 Kaphle A, & Hari P, *J Appl Phys,* 122 (2017) 165304.
37 Senol S D, Ozugurlu E, & Arda L, *J Alloys Compd,* 822 (2020) 153514.
38 Salameh B, Alsmadi A M, & Shatnawi M, *J Alloys Compd,* 835 (2020) 155287.
39 Bhardwaj R, Chae K H, & Goyal N, *Vacuum,* 178 (2020) 109446.
40 Dasari M P, Godavarti U, & Mote V, *Appl Ceram,* 12 (2018) 100.
41 Chanda A, Gupta S, Vasundhara M, Joshi S R, Mutta G R, & Singh J, *RSC Adv,* 7 (2017) 50527.
42 Singh M K, & Mehata M S, *Opt Mater,* 109 (2020) 110309.
43 Debnath P, & Mondal N K, *Environ Nanotec & Monit Manag,* 14 (2020) 100320.
44 Lam S M, Sin J C, Abdullah A Z, Mohamed A R, & Desalin, *Water Treat,* 41 (2012) 131.
45 Sadollahkhani A, Hussain Ibupoto Z, Elhag S, Nur O, & Willander M, *Ceram Int,* 40 (2014) 11311.
46 Sharma P, Singh M K, & Mehata M S, J *Mol Struct,* 1249 (2022) 131651.
47 Adam R E, Pozina G, Willander M, & Nur O, *Photo Nanostr & Fundam Appl,* 32 (2018) 11.